to be submitted to The Astrophysical Journal.

Draft of July 7, 2003

The Ionized Gas and Nuclear Environment in NGC 3783: IV. Variability and Modeling of the 900 ks *CHANDRA* Spectrum

Hagai Netzer,[1] Shai Kaspi,[1] Ehud Behar,[2] W. N. Brandt,[3] Doron Chelouche,[1] Ian M. George,[4,5] D. Michael Crenshaw,[6] Jack R. Gabel,[7] Frederick W. Hamann,[8] Steven B. Kraemer,[7] Gerard A. Kriss,[9,10] Kirpal Nandra,[11] Bradley M. Peterson,[12] Joseph C. Shields,[13] and T. J. Turner,[4,5]

ABSTRACT

[1]School of Physics and Astronomy, Raymond and Beverly Sackler Faculty of Exact Sciences, Tel-Aviv University, Tel-Aviv 69978, Israel.

[2]Physics Department, Technion, Haifa 32000, Israel

[3]Department of Astronomy and Astrophysics, 525 Davey Laboratory, The Pennsylvania State University, University Park, PA 16802.

[4]Laboratory for High Energy Astrophysics, NASA/Goddard Space Flight Center, Code 662, Greenbelt, MD 20771.

[5]Joint Center for Astrophysics, Physics Department, University of Maryland, Baltimore County, 1000 Hilltop Circle, Baltimore, MD 21250.

[6]Department of Physics and Astronomy, Georgia State University, Atlanta, GA 30303.

[7]Catholic University of America, NASA/GSFC, Code 681, Greenbelt, MD 20771.

[8]Department of Astronomy, University of Florida, 211 Bryant Space Science Center, Gainesville, FL 32611-2055.

[9]Center for Astrophysical Sciences, Department of Physics and Astronomy, The Johns Hopkins University, Baltimore, MD 21218-2686.

[10]Space Telescope Science Institute, 3700 San Martin Drive, Baltimore, MD 21218

[11]Astrophysics Group, Imperial College London, iBlackett Laboratory, Prince Consort Rd., London SW7 2AZ, UK

[12]Department of Astronomy, Ohio State University, 140 West 18th Avenue, Columbus, OH 43210-1106.

[11]Astrophysics Group, Imperial College London, iBlackett Laboratory, Prince Consort Rd., London SW7 2AZ, UK

[13]Department of Physics and Astronomy, Clippinger Research Labs 251B, Ohio University, Athens, OH 45701-2979.

We present a detailed analysis of the 900 ks spectrum of NGC 3783 obtained by *Chandra* in 2000–2001 (Kaspi et al. 2002). We split the data in various ways to look for time dependent and luminosity dependent spectral variations. This analysis, the measured equivalent widths of a large number of X-ray lines, and our photoionization calculations, lead us to the following conclusions: 1) NGC 3783 fluctuated in luminosity, by a factor ~ 1.5, during individual 170 ks observations. The fluctuations were not associated with significant spectral variations. 2) On a longer time scale, of 20–120 days, we discovered two very different spectral shapes that are noted the "high state" and the "low state" spectra. The observed changes between the two can be described as the appearance and disappearance of a soft continuum component. The spectral variations are not related, in a simple way, to the brightening or the fading of the short wavelength continuum, as observed in other objects. NGC 3783 seems to be the first AGN to show this unusual behavior. 3) The appearance of the soft continuum component is consistent with beeing *the only* spectral variation and there is no need to invoke changes in the absorber's opacity. In particular, all absorption lines with reliable measurements show the same equivalent width, within the observational uncertainties, during high and low states. 4) Photoionization model calculations show that a combination of three ionization components, each split into two kinematic components, explain very well the intensity of almost all absorption lines and the bound-free absorption. The components span a large range of ionization and a total column of about 3×10^{22} cm^{-2}. Moreover, all components are thermally stable and are situated on the vertical branch of the stability curve. This means that they are in pressure equilibrium and perhaps occupy the same volume of space. This is the first detection of such a multi-component equilibrium gas in AGN. 5) The only real discrepancy between the model and the observations is the wavelength of the iron M-shell UTA feature. This is most likely due to an underestimation of the dielectronic recombination rates in our model. We also note a small discrepancy in the calculated column density of O VI and discuss its possible origin. 6) The lower limit on the distance of the absorbing gas in NGC 3783 is between 0.2 and 3.2 pc, depending of the specific ionization component. The constant pressure assumption imposes an upper limit of about 25 pc on the distance of the least ionized gas from the central sourec.

Subject headings: galaxies: active — galaxies: individual (NGC 3783) — galaxies: nuclei — galaxies: Seyfert — techniques: spectroscopic — X-rays: galaxies

1. Introduction

NGC 3783 is a well known active galactic nucleus (AGN) with very strong X-ray absorption features. The object has been studied, extensively, with almost all X-ray instruments and most recently by *Chandra* (Kaspi et al. 2002, hereafter Paper I) and *XMM-Newton* (Blustin et al 2002). The 2–10 keV flux of NGC 3783 varies in the range $\sim$ (4–9) $\times$ 10^{-11} ergs cm^{-2} s^{-1}, and its mean 2–10 keV luminosity is $\sim$ 1.5×10^{43} erg s^{-1} (for $H_0 = 70$ km s^{-1} Mpc^{-1} and $q_0 = 0.5$). Paper I gives an extensive list of references and a comprehensive description of the history of all observations of the source including ground-based and UV (HST) observations. It also discusses the unique 900 ks *Chandra* data set obtained in 2000–2001.

These observations comprise of a relatively short observation performed in 2000 Jan, and five longer observations performed in 2001 Feb–Jun, separated by various intervals from 2 to 120 days (see §2) The paper contains numerous illustrations of the mean 900 ks spectrum, absorption line profiles and detailed measurements of many absorption and emission lines. Two other papers (Gabel et al., 2003a; Gabel et al., 2003b) discuss the HST and FUSE spectra of the source.

The purpose of the present investigation is to analyze the 900 ks spectrum of NGC 3783 and to model the X-ray gas with emphasis on the absorber's properties. There were several previous attempts to model the source. Perhaps the most detailed work, so far, is by Kaspi et al (2001) who attempted to fit the 56 ks spectrum obtained with *Chandra* in 2000. Their most successful model is made of two absorbing shells both outflowing from the central source with velocity of $\sim$ 600 km s^{-1}. The gas was assumed to be turbulent with internal turbulent motion of $\sim$ 250 km s^{-1} and the two shells have similar column density and different ionization parameters. The model produces a satisfactorily explanation to the observed intensity and equivalent width (EW) of many but not all emission and absorption lines. A major limitation of the Kaspi et al. (2001) work was the limited signal-to-noise (S/N) of their data and hence the large uncertainty on the model parameters. In addition, the data quality, and the observation duration, did not allow a meaningful time-dependent analysis.

The superb quality of the 900 ks *Chandra* data set allows a more detailed study of the physics and dynamics of the X-ray gas in NGC 3783. In §2 we describe the multi-phase X-ray spectrum discovered by the new observations and in §3 we explain the various ways we measured and modeled the spectrum. §4 contains a discussion of the new findings and §5 summarizes the new results.

2. The two-state X-ray spectrum of NGC 3783

Full description of the 900 ks data set is given in Paper I. In short, there are 5 observations of about 170 ks each separated by various times, from 1 to 90 days. These were combined with the earlier (GTO, 2000) 56 ks data set (Kaspi et al. 2001) to give a net total on target integration of 888.7 ks. All measurements in Paper I refer to this combined spectrum. The MEG and the HEG first order spectra were combined to a single spectrum, binned to 0.01Å, which served as the main source for the EW measurements. Third order data from the MEG were also used to investigate several short wavelength line profiles and compare them with the first order long wavelength line profiles. It was found that most resolved absorption lines (e.g. O VII, Ne IX and Si XIV lines) are made of at least two kinematic components, one centered at -500 ± 100 km s^{-1} and the other at around -1000 ± 200 km s^{-1}. The overall absorption covers the velocity range of 0 to -1600 km s^{-1} (e.g. paper I Fig. 5 & 10).

A major goal of the present work is to investigate partial data sets of the 900 ks spectrum. We subdivided the data in various ways to check for spectral variations as a function of source luminosity and time. This was done for short (within individual 170 ks observations) as well as for long (between observations i.e. 20–90 days) time scales. The short time-scale behavior of NGC 3783 is illustrated in Fig. 1 where we show the short wavelength (2–10 Å) flux as a function of time for all observations binned in intervals of 3170 sec. The diagram also shows the softness ratio light-curve defined as the flux in the 15–25Å band divided by the flux in the 2–10 Å band. Consider first the total 2–10 Å flux. We find that it varied by about 50% over the 170 ks interval during all observations. However, there is no sign of significant spectral variations (i.e. softness ratio) during individual observations. Thus, the data show a constancy of the spectral energy distribution (SED) over 1–4 days time scales (observations 2090 and 2091 are consecutive with total duration of about 4 days). To further test this finding, we have also extracted partial spectra from individual 170 ks data sets combining, separately, high and low flux data. In no case have we found noticeable spectral variations corresponding to those flux variations. We also note that Behar et al. (2003) did not find spectral variations in NGC 3783 over approximately three days during Dec. 2001, when the XMM-Newton observed the source.

Contrary to the above, there is a *very significant* change of SED on longer time scales. In particular, there is a major change in SED and in softness ratio between observations nos. 2092 and 2093 (20 days separation) and observations nos. 2093 and 2094 (90 days separation). As shown in Fig. 1, observation no. 2093 shows a higher mean count rate but exhibits a much softer spectrum. Direct comparison of the spectra of observations nos. 2093 and 2094 shows that during the 90 days period the low energy part ($\lambda > 15$Å) has decreased

in flux by a factor of ~ 4 compared with the much smaller decrease (~ 1.5) of the shorter wavelength continuum. The opposite change has occured between observations no. 2092 and no. 2093. Most important, the softness ratio variations *are not* simple luminosity-related effects. For example, the 2–10 Å count rate in the middle of observation no. 2093 (Fig. 1) is, in fact, a little lower than the 2–10 Å flux toward the end of observation no. 2094. Yet, the softness ratio of the first is significantly higher than that of the second. A similar effect is seen in observation 2093 where the 2–10 Å count rate varied by about 50% during the observation yet the softness ratio is practically constant.

To further examine this point, we have divided the entire data set into groups of high and low softness ratios. We find four observations (2090, 2091, 2092 and 2094) with low softness ratio and two (0373 and 2093) with high softness ratio. We refer to these as the "low-" and "high-state" observations, respectively. The names were chosen to emphasize the fact that the high softness ratio spectrum is also of higher luminosity. We find no significant differences between the mean spectra of the four individual low-state observations (except for a small intensity variations). Similarly we find no significant differences between the mean spectra of the two high-state observations.

Fig. 2 is a more detailed example of this phenomenon. It shows the softness ratio as a function of the 2–10 Å flux for all the data using 3170s bins. The separation into two group is apparent and a standard KS statistical test confirms its significance. We have also looked at the possible linear correlation of the softness ratio with the 2–10 Å flux in each of the groups. In the low softness ratio group, we find a positive slope which is different from zero by more than $> 3\sigma$. The linear regression line shown in the diagram is clearly not connecting the low and the high softness ratio groups. As for the high softness ratio group, no significant correlation of softness ratio with flux was found. We conclude that the X-ray spectrum of NGC 3783 fluctuates between two very different states with different softness ratios. The combined spectra of the two are shown in Fig. 3 and much of the rest of this paper is devoted to the analysis of this unusual behavior of NGC 3783.

3. Spectral analysis and modeling

3.1. Spectral differences between the high and the low states

We have investigated the unusual observed variations in the spectrum of NGC 3783 in attempt to understand their nature and their origin. In particular, we have attempted to answer the question of whether they are due to the response of the absorbing gas to the observed continuum variations.

There are two ways to answer the above question: one by a direct and detailed spectral comparison and the other by modeling the two observed spectra trying to establish the origin of the observed differences. Fig. 4 is an example of the first approach. The diagrams shows a comparison of the low and the high state spectra after applying a simple scaling factor to the first to match the local continuum of the second. As explained, the required scaling is wavelength dependent. Therefore, we divided the two spectra into limited bands and applied, to each, the required factor. The two examples shown here, and all others we have examined, illustrate that except for a luminosity scaling the two absorption line spectra are indistinguishable within the uncertainties that are of order 10% for the low-state spectrum and about twice that for the high-state spectrum (the somewhat weaker looking lines of low ionization species in the high-state spectrum, e.g. around 7Å, are well within the noise). Table 1 gives measured EWs for several key absorption lines (see §3.2.3) in the high and the low state spectra. Again, the small differences between the two spectra are well within the uncertainties. We proceed under the assumption of no variations in the line EWs between the two states and comment, in §4.1, on the implications of variations that are within the observational uncertainties.

3.2. Spectral modeling

The second and complementary approach for investigating the spectral changes is by detailed modeling of the absorbing and emitting gas. The idea is that the gas is photoionized by the central X-ray source and the observed spectra represent its physical state during the two states. The principles and the ingredients of such modeling were outlined in Netzer (1996) and previous applications to the case of NGC 3783 were discussed by Kaspi et al. (2001). Here we summarize the basic method and explain its application to the high and the low-state spectra of NGC 3783.

3.2.1. General method and model ingredients

The X-ray gas is assumed to be photoionized by a central source and in photoionization and thermal equilibrium (see §4 for discussion of the last point). Modeling is done by ION2003, the 2003 version of the code ION (Netzer 1996). The code includes all relevant atomic processes and computes the ionization and the thermal structure of the gas as well as line intensities and EWs for more than 2000 X-ray lines. This is done for various geometries, from a single cloud to a multi-component expanding atmosphere. The basic parameters of the model are the gas density (assumed to be in the range 10^{2-6} cm^{-3} - see justification in §4),

the hydrogen column density (N, in units of cm^{-2}), the covering factor, the gas composition, turbulent motion (§3.2.2) and the oxygen ionization parameter (U_{OX}) defined over the energy range 0.54–10 keV. As explained by Netzer (1996), and discussed further in George et al. (1998), this choice of ionization parameter (compared with, for example, U_X defined over the 0.1–10 keV range) gives the most meaningful definition of the X-ray ionizing field in AGN. As for the covering factor, we distinguish between the emission covering factor ($\Omega/4\pi$) applicable to the emission line gas, and the absorption (line-of-sight) covering factor which can be different and is applicable to the absorbing gas. The following "solar composition" was used throughout this work:
H : He : C : N : O : Ne : Mg : Al : Si : S : Ar : Ca : Fe =(10^4 : 10^3 : 3.7 : 1.1 : 5 : 1.1 : 0.37 : 0.03 : 0.35 : 0.16 : 0.033 : 0.023 : 0.4) $\times$ 10^{-4} (note the reduced oxygen abundance compared with older estimates).

The incident continuum is taken to be the broken power-law defined in Kaspi et al. (2001, Table 4). The only changes we have experimented with are related to the slope of the 0.1–50 keV continuum. As discussed below, the UV part of the source can be different from the one assumed here with important implications for the UV absorption lines. This will be investigated in a forthcoming paper. The effects of the UV continuum on the X-ray gas are of far less importance and we consider this choice of SED to be adequate for the present analysis.

The models calculated here are entirely self-consistent and are not simple attempts to fit the observed spectra by measuring line EWs and deducing column densities for the different ions. We search for the combination of real physical components that can be produced in nature in an environment where low density gas is exposed to a typical AGN continuum. These components are then combined, in a realistic way, taking into account screening, attenuation of the radiation field, etc.

3.2.2. Multi-component models

We have examined the hypothesis that the observed spectral changes are consistent with pure opacity variations, i.e. no variations in the intrinsic SED except for wavelength independent luminosity variations. We start by calculating a variety of models in order to mimic the low-state spectrum. Each model is made of several emission and absorption components. The absorbers are specified by U_{OX}, N and the absorption (i.e. line of sight) covering factor which is assumed to be the same for all absorbers (see however discussion in §4). The absorbers are assumed to be aligned such that the observed spectrum is the result of the intrinsic continuum passing through all absorbers. The emission components are

specified by their U_{OX} and N (that are not necessarily identical to those of the absorbers), their covering factor and by whether or not they are occulted by the absorbing gas.

The dynamics and kinematics of the absorbing gas are important factors in comparing the data with the model results. Following numerous UV observations, and our analysis in paper I, we assumed internal motion in the gas which is much larger than the thermal motion. This "turbulent velocity" is assumed to have a Doppler profile and the velocity quoted is the Doppler b parameter. Paper I shows that all absorption lines with good S/N and sufficient resolution (the lines of O VII, Ne X, Mg XII and Si XIV) can be characterized by two kinematic components. The central velocities of the two are between -400 and -600 km s^{-1} and between -1000 and -1300 km s^{-1}, relative to the systemic velocity. A good representation of the observations can be obtained with two Doppler profiles each with $b \simeq 250$ km s^{-1}.

The relative EW and covering factor of the two velocity components are critical to our modeling of the source. The observations show that the EW ratio of the two velocity components is about 1:0.7, where the lower outflow velocity componet is the one with the larger EW. Since the separation into components is seen in several saturated lines, it can be interpreted as due to different absorption covering factors. In this case, the lower outflow velocity component has a covering factor of 0.8–1.0 and the larger velocity one a covering factor of 0.6–0.8. However, the composite profiles inclue also unsaturated lines that seem to have similar shapes. In this case, the different EWs are due to different column densities. We cannot distinguish between the two possibilities since we do not have high quality high resolution profiles for many weak lines. Given these uncertainties, we investigated two cases where the relative column densities for the two velocity components are in the ratio of 1:0.7. In one case the covering factor of all absorbers is unity and in the other case it is of order 0.8.

In summary, each "ionization component" of the models presented in this paper is made of two "kinematic components". For the outflow velocities we chose -500 and -1000 km s^{-1} and for the turbulent velocity 250 km s^{-1} for both components. This implies that the total derived column density of a certain ionization component is *the sum* of the column densities in the two kinematic components, even for saturated lines, since there is very little velocity overlap between the two. Given those assumptions, we have used the EWs measured in Paper I, combined them with a few new measurements, and translated the EWs into column densities and optical depths. The more important lines that were used to constrain our models, and their adopted column densities, are listed in Table 2.

3.2.3. The silicon and sulphur line method

A major clue for the conditions in the absorbing gas is obtained from EW measurements of various 5–7.1 Å lines. This wavelength range contains lines from Si VII to Si XIV as well as the strongest lines of S XV and S XVI. Most lines are unblended with little contamination from other species. The range of ionization and excitation is very large and represents the ionization of almost all line producing ions in the spectrum. The column densities deduced from these EWs, assuming the two component profiles, are given in Tables 1 & 2. The atomic data for the lines are known either from standard calculations (f-values for the H-like and He-like transitions) or from the recent work of Behar and Netzer (2002) discussing the inner-shell lines of silicon, sulphur and other elements.

We have developed a simple algorithm to compare the measured optical depths of all the observed silicon and sulphur lines with the results of the photoionization calculations. The algorithm operates on a large grid of computed models that contains theoretical optical depths for a large range of ionization parameters and column densities. It picks combinations of up to 4 models and compares the *combined* optical depth for every one of the chosen lines, with the values measured from the stronger (i.e. the larger column density and lower outflow velocity) observed kinematic component. The best combination of models is obtained by minimizing the differences between the observed and the calculated optical depths in 10 lines (the 9 silicon and sulphur lines listed in Table 1 plus a line of Si VII). The result is a list of up to four models, with various column density and U_{OX}, whose combination gives the best match to the observed column densities. Using this procedure we find that at least three ionization components (i.e. six kinematic components) are required to fit the data to within the observational accuracy.

Experimenting with various modifications of the method suggests that there are several combinations of three or four ionization components that give similar quality fits to the observed optical depths of the silicon and sulphur lines. All combinations share the same general properties in a sense that they all require at least three very different sets of physical conditions (i.e. ionization parameters) and three similar column densities. A generic model with the required properties is the following three-component model (all column densities refer to the total column of the two kinematic components): 1. A low ionization component with $\log(U_{OX}) = -2.4 \pm 0.1$ and $\log(N) = 21.9 \pm 0.1$ 2. A medium ionization component with $\log(U_{OX}) = -1.2 \pm 0.2$ and $\log(N) = 22.0 \pm 0.15$ 3. A high ionization component with $\log(U_{OX}) = -0.6 \pm 0.2$ and $\log(N) = 22.3 \pm 0.2$. The uncertainty in the column and ionization of the low ionization component represents, more than anything else, the uncertainty on the slope of the ionizing continuum. Relaxing this condition allows a somewhat smaller column demsity (see §3.2.4). The larger uncertainties on the parameters of the higher ionization

components are due to the fact that gas with such properties produce similar EWs for medium (e.g. Si XI) and high (e.g. Si XIV) ionization lines over a larger range of ionization parameters and column densities. The three theoretical ionization components are plotted over a large wavelength range in Fig. 5, and a more detailed view of the 4.5–7 Å range is shown in Fig. 6.

3.2.4. Intrinsic continuum and global model properties

The next step is to test the combination of components that best fit the optical depths of the 5–7.1 Å silicon and sulphur ions over other wavelength bands. This requires to define more precisely the shape of the underlying ionizing continuum. In principle this is an easy task since one can measure directly the slope of the short wavelength continuum, where bound-free absorption is negligible. However, Fig. 5 clearly shows that two of the generic absorbers are characterized by large opacity which affects the shape of the apparent underlying continuum at wavelength as short as 4–5 Å, making a unique determination of the 2–5 Å continuum slope (the part available for the grating observations) a complicated task. More specifically, the exact O VII column density in the lowest-ionization component strongly influences the short wavelength continuum shape and the uncertainty on this column translates to an uncertainty on the slope.

Given the above constraints on the model properties, and the observed 2–5 Å continuum, we have experimented with various power-law continua requiring that both the short wavelength continuum and the measured EWs of the silicon and sulphur lines, are within the observational uncertainties. All fits were performed on the low-phase spectrum. We found that a single power-law with a photon index of $\Gamma = 1.65 \pm 0.15$ is the best overall representation of the low-state spectrum. We note that the data quality cannot exclude the possibility of some steepening of the intrinsic continuum at long ($\lambda > 20$Å) wavelengths.

Another uncertainty on the intrinsic SED comes from the fact that some of the high energy photons are likely to be produced far away from the source, due to Compton scattering and reflection of the central continuum radiation. This can be very noticeable in faint sources, like NGC 3516 during 2000 (see Netzer et al. 2002). Scattering by low ionization gas is strongly wavelength dependent and, for NGC 3783, can amount to a change of ~ 0.1 in the derived value of Γ. As a result, we might have overestimated the column density of the lowest ionization component (the only component with significan influence on the slope of the short wavelength continuum) which would results in overestimating the column densities of low ionization species such as O V and O VI. §4.1 contains some discussion about the lowering of the column density in our low U_{OX} component and a more detailed examination

of this effect is deferred to a separate paper (George et al. 2003, in preparation).

Given the chosen continuum and the three ionization components, we have calculated a combined multi-component model that covers the entire wavelength range. The model includes two kinematic components for every ionization component and the theoretical spectrum is compared with the observed low-state spectrum in Fig. 7. The results are very good. In fact, we could not find another combination of models (three or more absorbers) that is significantly better than this combination. It gives a good overall fit not only to many lines of all elements but also for the strong bound-free edges. Thus, the constraints on the 5–7.1 Å silicon and sulphur lines are enough to completely specify a model for the entire spectrum.

3.2.5. Comparison of the high and the low state specta

As demonstrated above, the low-state absorption spectrum of NGC 3783 can be satisfactorily explained by the chosen combination of line-of-sight absorbers. The agreement with the observations is very good for all lines with $\lambda < 15$Å. However, there is a noticeable discrepancy at around 16Å. At this wavelength range there are two main opacity sources, the O VII bound-free continuum (edge at 16.7Å) and the iron M-shell UTA feature (Behar, Sako & Kahn 2001). The photoionization calculations suggest a disagreement between the two in the sense that the strongest observed iron lines are due to ions that indicate lower ionization compared with the strongest observed oxygen lines. Thus the peak UTA absorption corresponds to Fe VIII–Fe X while this level of ionization of iron corresponds, according to our grid of models, to most oxygen being in the form of O III–O VI. Yet, the observations indicate that most of the oxygen bound-free absorption is due to O VII. The possible origin of this discrepancy is discussed in §4.

Regarding the $\lambda > 19$Å region, the comparison between the model and the observations is limited by the poorer S/N. While the model shown in Fig. 7 is consistent with the data, several calculated absorption lines in this range, in particular those due to O V and O VI, seem to be stronger than the ones observed. This may be a real shortcoming of the model (see comments in §3.2.4 and in §4). It may also be the result of the assumed absorption covering factor. As already mentioned, line-profile analysis suggest a mean (over the line profile) covering factor of 0.7–1.0. Yet, all models considered so far assumed the extreme case of an absorption covering factor of unity. The "leakage" of the incident continuum makes little difference at short wavelengths except for a need to somewhat decrease the assumed Γ since the absorbed continuum is steeper than the intrinsic continuum. However, leakage can influence the comparison at long wavelengths much more. This is illustrated in Fig. 8 which shows a model with $\Gamma = 1.5$ and a line-of-sight covering factor of 0.85. Indeed, the

agreement at long wavelengths is much better. The differences between the two assumed slopes and covering factors are well within the model uncertainties.

We have attempted to model the high-state spectrum by assuming the same ionization components and by changing the luminosity and the ionization parameter by the factor inferred from the observed increased luminosity in the short wavelength continuum (~ 1.5). The result is a very poor fit to the long wavelength continuum luminosity and to the intensities of many lines. The reason is that such a small luminosity change results in an opacity change which is too small to account for the very large difference (factor ~ 4) between the low and the high state spectra at long wavelengths. This means that the high and the low state spectra are inconsistent with the assumption of a simple response of the gas to continuum luminosity variations.

Contrary to the above, there is a simple and satisfactory solution for the high-state spectrum that involves the appearance of an additional continuum component. This second, long wavelength component ("soft excess") appears only during high state. We have therefore tried to model the high-state continuum by two powerlaws: the low-state powerlaw ($\Gamma = 1.6$) and a much steeper component with $\Gamma = 3.2$. The combination of the two that best explains the high state spectrum requires the $\Gamma = 3.2$ component to emit 40% of the flux of the $\Gamma = 1.6$ component at 12.398 Å (1 keV). This is not a unique combination and similar quality fits can be obtained by somewhat different combinations of slope and normalization. The two chosen continua are shown in Fig. 3 where they are compared with the high and the low state spectra. Given the two component continuum, we find a very good agreement for the high-state line and continuum spectrum by assuming *no opacity variations.* The quality of the fit is similar to the low-state fits shown in Figs. 7 & 8.

To further illustrate this point we show in Fig. 9 a comparison of the division of the high-state spectrum by the low-state spectrum (binned to reduce the noise) with the division of the two assumed continua. The diagram shows that all remaining spectral features are entirely consistent with the noise. The S/N in this diagram is not high enough to completely rule out some opacity-like variations at long wavelengths. In particular, there is some excess emission near the O VII and O VIII recombination edges that may hint to extra emission in the high-state spectrum (note that we do not expect the emission features to disappear by this division). However, such opacity variations must contribute very little to the observed long-wavelength spectral variations.

Finally, the emission-line spectrum of NGC 3783 can be explained by assuming X-ray emitters with the properties found for the ionized absorbers. The emitted line photons are are probably observed through the absorber, as indicated by the combined emission-absorption profiles of several resonance lines. The model emission is problematic at around

21.8Å, where it fails to reproduce the intercombination O VII line. The required emission covering factor is about 0.1 (see §4.1) consistent with the value of approximately 0.05–0.15 obtained by Behar et al. (2003).

4. Discussion

The main new findings of this work are the large increase in flux between the low and the high-states and the very little, if any, corresponding changes in the absorber's properties. The central source in NGC 3783 fluctuates between two such flux states on a 20–120 days time scale and the best description of the observed variations is the appearance and disappearance of a "soft excess", low energy continuum component. These lead to important conclusions regarding the nature of the continuum source. Other important conclusions are the multi-component nature of the absorber and the large range of ionization. Below we discuss some interpretations.

4.1. Physical properties of the absorbing gas

We found that three ionization components with different properties and a large range of ionization, are required to fit the spectrum of NGC 3783. Each of those components is split into two kinematic components, as implied by the line profile observations. The three "generic absorbers" of our model are listed in Table 3 and shown in Figs. 5 & 6. As explained above, the number of real components and the exact values of U_{OX} and N are not very meaningful since several somewhat different combinations of ionization components give equally good fits. Rather, the values chosen here give good ideas of the mean required ionization parameters and the total required column density. Our modeling of the low-state spectrum assumes a single power-law X-ray source. However, the S/N of the long wavelength spectrum is not high enough to completely rule out the presence of an additional softer continuum component, similar to the one seen during high states but of much lower luminosity. We also note the little or no response of the absorbing gas to the short ($\sim$ 2 days) time scale continuum variations and thus what we measured and modeled represent some time-averaged spectral properties.

The main difference between the present model and the one given by Kaspi et al. (2001) is the presence of the lowest ionization component. This is not surprising since that work tried to fit the high-state spectrum by a single powerlaw continuum. They were not aware of the two-state spectrum, did not have the additional information on the long wavelength,

more neutral oxygen lines, and their S/N at $\lambda > 18$Å did not allow a meaningful continuum fitting at those wavelengths. Thus they assumed a component with a strong O VII bound-free edge but very little absorption at longer wavelengths, i.e. continuum recovery at wavelengths greater than about 18Å. Our new observations do not show such a recovery. In fact, the absorption in the long wavelength region of the low-state spectrum is dominated by features of K-shell carbon and nitrogen and L-shell nitrogen and oxygen.

Perhaps the largest observed discrepancy between model and observation is due to absorption by the iron M-shell UTA. This feature has been observed in several other AGN (Steenbrugge, K.C. et al and references therein) with similar shape and central wavelength. Its smooth shape is due to the large number of absorption lines of many iron ions and the wavelength of largest absorption is ionization dependent. The central observed wavelength of the feature in NGC 3783 is at around 16.4Å suggesting that most of the contribution is due to Fe VIII–Fe X. For the assumed SED, this corresponds to gas whose dominant oxygen ions are O III–O VI. In our modeling, most long wavelength absorption is due to the component with $\log(U_{OX}) = -2.4$ (Fig. 5). The dominant ions in this components are O VI–O VII and Fe X–Fe XII. This corresponds to peak UTA opacity at around 16.1Å. As shown in Fig. 7, the model fits the observed oxygen lines and continua reasonably well but misses badly the position of the UTA absorption.

We have experimented with various other models to try to eliminate this discrepancy. For example, an overabundance of iron relative to oxygen may decrease the iron level of ionization due to the increased iron opacity. Experimenting with iron abundance which is three times larger resulted with changes that are not large enough to explain the observed discrepancy. We have also experimented with models that include several low ionization components, instead of the single low U_{OX} component shown here. This, again, gave very little improvement. It seems that the apparent conflict between the oxygen and iron ionization cannot be resolved by these models and we suggest two alternative explanations.

1. The absorbing gas in NGC 3783 may not be in ionization equilibrium due to its low density and the rapid flux variations on time scales that are shorter than the recombination and ionization time scales. This is probably not very important for the short wavelength flux since its variability time scale is short and the amplitude not very large. The gas responding to this continuum is probably at some mean level of ionization. This however is not the case for the soft excess continuum which varies on a much longer time scale with a much larger amplitude. This can contribute, significantly, to the ionization of the lower ionization species yet different ions react on different time scales and the gas may never reach an equilibrium. Since all our models assume steady state gas, they may not be adequate to describe the absorbing gas properties. In par-

ticular, the iron and oxygen recombination times may be different enough to result in gas where iron is less ionized or oxygen is more ionized compared to the equilibrium situation. The complicated issue of time dependent ionization is beyond the scope of this paper.

2. The ionization balance of iron depends critically on low temperature dielectronic recombination (DR) rates that are not well known for the iron M-shell ions. Experience with L-shell iron ions, whose DR rates have been measures and computed recently (Savin et al. 2002 and references therein), shows that in almost all cases the previous low temperature DR rates were consistently smaller than the newly calculated values. Assuming a similar effect in the M-shell ions, we can envisage a situation where, in the absence of realistic DR rate, the entire ionization balance of iron is shifted toward higher ionization. Thus, more realistic low temperature DR rates may bring models to better agreement with the observations. We note that low temperature DR rates are also not available for the magnesium and silicon ions that we have modeled. For some of these ions (Mg VIII and Mg IX) these are probably not very important and for others (the relevant silicon ions) the situation is less clear (D. Savin, private communication). We note again the good agreement between the calculated EWs of these lines and the EWs of numerous other lines observed in the spectrum.

An interesting and somewhat problematic issue is the abundance of O VI, which can also be clearly observed in the far UV (Gabel et al. 2003a; Gabel et al., 2003b). Paper I found even the Kα line of O VI undetectable with the current S/N. However, revisiting this measurement more carefully, and with more accurate atomic data, we can in fact detect several O VI lines. We now measured two of those lines, that are probably saturated, and obtained a lower limit of $10^{17.0}$ cm^{-2} on the column density of O VI. This is much higher than the RGS measured value of $10^{16.0\pm0.3}$ cm^{-2} (Behar et al. 2003). Moreover, the model prediction ($10^{17.96}$ cm^{-2}) is even larger. Such a large value is problematic for several reasons. It may be in contradiction with the UV observations of the source (see below), it is much larger than the values obtained from the RGS observations, and it results in a prediction of a strong absorption line at around 21.87 Å which is not seen in the spectrum (Fig. 7, the absorption line underneath the O VII intercombination line).

We explain the discrepancy in the measured *Chandra* and *XMM-Newton* values for the O VI column density through the crowded region of the spectrum where O VI Kα resides. In particular, the lower spectral resolution of the RGS makes it extremely difficult to resolve the weak O VI absorption line at 22.01 Å in the presence of the bright O VII forbidden emission line (22.10 Å). We also wish to note that with the lack of laboratory measurements for the O VI wavelengths, high-resolution astrophysical spectra such as the present one constitute

the best available determination of these wavelengths. The present spectrum together with the assumption that O VI is outflowing at the same velocity as O VII places the O VI Kα line at 22.01 $\pm$ 0.01 Å in the rest frame. This value is in agreement with our model wavelength of 22.005 Å calculated with the HULLAC atomic code as well as with the value measured in NGC 5548 (Steenbrugge et al., 2003), but is somewhat different from the value of 22.05 Å calculated by Pradhan (2000) using the R-matrix method.

A column density of 10^{17} cm^{-2} or lower for O VI is also inconsistent with theoretical predictions based on modelling the abundances of Mg VIII, Si VIII and O VI. This is illustrated in Fig. 10 where we show the calculated fractional abundance of oxygen, silicon and magnesium ions as a function of U_{OX} for an incident continuum similar to the one assumed here. The diagram shows the very similar fractional abundance of O VI, Mg VIII and Si VIII as a function of ionization parameter. Using the measured EW of the Si VIIIλ 6.998 line, which is an unblended, easy to measure feature, we can use Fig. 10, and the assummed silicon-to-oxygen abundance ratio, to derive an estimate for the column density of O VI. This number is very close to the model prediction. The situation is more complicated regarding magnesium since several of the relevant lines, around 9.4Å are blended with neon lines. However, we could obtain an estimate of the EW of the Mg VIII λ9.506, 9.378 lines that are good enough to constrain the Mg VIII column density. The O VI column density based on this measurement is, again, much larger than 10^{17} cm^{-2} and in good agreement with the model prediction.

Finally, we have looked for the lowest O VI column density allowed by the observations if we remove the constraint imposed by the short wavelength continuum slope (§3.2.4) and keep the ionization parameter unchanged. This means finding the lowest column density log(U_{OX})=-2.4 component that is still consistent with the measured EWs of the 5–7.1 Å silicon and sulphur lines. We found tht column to be log(N) $\simeq$ 21.7 for the low-state spectrum and log(N) $\simeq$ 21.6 for the high-state spectrum. These minimum columns are consistent with the uncertainties give in Table 1. Under these assumptions, the column density of O VI in the low-state spectrum can be as low as $10^{17.76}$ cm^{-2}. This column is large enough to produce saturated O VI lines at 21.01 and 21.87 Å. It also requires a much harder continuum ($\Gamma = 1.4$).

4.2. Outflow velocity and covering factor

Some of our chosen model parameters are based on measured profiles of several absorption lines that were shown, in Paper I, to include at least two components with different ouflow velocities. The measurements in paper I also show that the relative EWs of the two

components seems to be ionization independent and that most of the lines used for the profile analysis were heavily saturated. This suggests that the apparent optical depths of those lines are determined by covering factor rather than the line opacity, similar to the case in many UV AGN absorbers (e.g. Barlow, Hamann & Sargent 1997; Arav et al. 1999). The covering factor of the lower outflow velocity components of the O VII, Ne X and Si XIV lines is in the range 0.8–1.0. The covering factor of the larger velocity component of the same lines, assuming saturated profiles, is 0.6–0.8. We also note that the large number of iron lines near the UTA center gives an independent estimate of the covering factor which is at least 0.85.

Fig. 8 shows that models with a covering factor less than unity give similar quality fit to the data. Using the silicon and sulphur lines (as in §3.2.3), we find three ionization components are again required, each with parameteristics similar to those listed in Table 3. The only difference is the need to assume a somewhat harder ionizing continuum. The fit to the long wavelength lines is somewhat better than the one produced by the full covering models but given the S/N at those wavelengths, this is not a strong conclusion. Thus, the data-model comparison cannot constrain covering factor beyond the actual observations. The most important conclusion is that the covering factor is similar in low (e.g. O VII and the iron UTA) and in high (e.g. Si XIV, Ne X) ionization lines.

4.3. Density, location and thermal stability of the absorbing gas

Our measurements and analysis are consistent with no variations in the absorber's properties on a 1–4 days time scale with indications for a much longer period of no spectral changes, perhaps a few months (note that there is no evidence for any significant narrow $<$ 1 Å spectral features in the ratio spectrum shown in Fig.9). The reason we cannot constrain the variability of the absorbers on short time-scales are the fast, small amplitude fluctuations in the luminosity of the central source (maximum amplitude of about a factor 2). Because of this, the little or no spectral variations may be due to the fact that the gas level of ionization reflects the *time averaged* ionizing luminosity rather than very long ionization or recombination times. The no change conclusion depends therefore mostly on the direct comparison of the low and the high state spectra and thus on the S/N is the lower quality spectrum used for the comparison (the high state spectrum).

To further examine this point, we have calculated the expected theoretical spectrum of the high state continuum assuming that the absorbing gas responds instantly to the continuum variation. This would be the case for a high density line-of-sight gas. The initial conditions are those assumed for the low state continuum and the change in the SED as described earlier (the two component X-ray continuum) with the assumption that the soft

excess can be extrapolated to low energies (up to 40 eV) with the same slope. The flux increase was assumed to be a factor 1.5 at 4 Å (see Fig. 3).

Fig. 11 shows two theoretical spectra. The low state spectrum (in blue) is the same model shown in Fig. 7. The high state spectrum (in red) is the new calculated model. The two are very different. In particular the Si VII, Si VIII and Si IX lines are almost completely disappeared from the theoretical high state spectrum. The changes are due to the large flux increase at long wavelengths that affect mostly the lowest ionization component (U_{OX} has increased by a factor close to 2 and U_X by a factor of 6.6). The observed variation, if any (Table 1 and Fig. 4), are much smaller than the predicted, strengthening the assumption of little or no response to continuum variations. An even stronger conclusion is obtained from the fact that the observed differences between the high and the low states, at long wavelengths, are far too large to be explained by simple opacity variations.

Given all the above, we have attempted to put limits on the density and location of the absorbing gas assuming no response to continuum variations on a 10 days time scale for all absorbers. Using the temperatures from the models, we derived the following limits on the electron density (n_e) and distance from the central source (D): For the $\log(U_{OX}) = -2.4$ component, $n_e < 5 \times 10^4$ cm^{-3} and $D > 3.2$ pc. For the $\log(U_{OX}) = -1.2$ component, $n_e < 10^5$ cm^{-3} and $D > 0.63$ pc. For the $\log(U_{OX}) = -0.6$ component, $n_e < 2.5 \times 10^5$ cm^{-3} and $D > 0.18$ pc. The recombination times used are averages of the recombination times for the dominant oxygen and silicon ions in the three components (Behar et al. 2003), by associating the soft X-ray line emission and absorption, have suggested that the outflow is located at a distance of a few pc away from the source and that it is extended beyond 10 pc).

A significant new aspect of our model is the fact that the product $n_e \times T$ is the same, to within a factor of less than 2, in all absorbers. This raises the interesting possibility that all components are in pressure equilibrium and they all occupy the same volume of space. To test this idea, we have calculated thermal stability curves ($\log(T)$ vs. $\log(U_{OX}/T)$ for the low-state continuum under various assumptions. We have kept the UV SED unchanged and varied Γ(0.1–50 keV) over a wide range. We have also investigated the possibility of a line-of-sight attenuation by the absorbing gas. This can be relevant for the situation under study since, even in the simplest geometry, two of the absorbers do not have a clear view of the central radiation source. Screening by the lowest U_{OX} component is the most important since this gas modifies the transmitted spectrum much more than the other components (see Fig. 5). Three stability curves calculated in this way are shown in Fig. 12 and the location of the three ionization components are marked on the curves. The exact location depend on the details of the assumed SED, the gas metallicity and opacity.

The interesting feature of the stability diagram is that all radiation fields considered

here result in extended, almost vertical parts between $T \simeq 3 \times 10^4$ K and $T \simeq 2 \times 10^6$ K. The $\Gamma = 1.6$ curve has a more extended part since the Compton temperature of this continuum is higher due to the higher mean energy of the radiation field. Attenuation of the central SED by the NGC 3783 most extreme absorber is, indeed, important but does not change the main result that, given the uncertainties on the SED and composition, all three ionization components lie on the stable part of the curve. We also note that, while here we kept the gas composition constant, the details of the stability curve are abundance dependent. Needless to say, very different shape curves will be obtained for significantly different SEDs.

The idea of an additional intermediate stable region (between the cold and the hot branches) along the thermal equilibrium line of AGN radiation field, where "warm" ($few \times 10^5$ K) gas can survive, is not new. It has been discussed by Marshall et al. (1993) in their study of the multi-phase medium in NGC 1068 and later by many others. Reynolds & Fabian (1995) discussed the stability criteria and noted the narrow range of ionization parameter allowed for warm absorbers. Hess et al (1997) discussed the various parameters governing the stability curve (metallicity and more). Komossa and collaborators (e.g. Komossa & Fink, 1997; Komossa & Meerschweichen 2001) calculated many such curves, for different SEDs and metallicities, and discussed the location of warm absorbers as well as the possible link between the NLR and the X-ray gas. Krolik & Kriss (2001) considered multi-phase warm absorber winds and noted the various locations of stable, over-heated and over-cooled gas. Kinkhabwala et al. (2002) re-visited the thermal stability issue in NGC 1068 and showed that a wide range of U_{OX} is needed to account for the observed X-ray emission lines. Chelouche & Netzer (2003) investigated the changes in the stability criteria for clouds with large internal line radiation pressure.

Most of the earlier works focused on the parts of the curved allowed for the warm X-ray gas with regard to the general stability conditions or to the location of a certain absorber observed in a certain source. Our work shows that three very different aborbers in a certain source can all occupy extended, stable parts of the curve where the gas pressure is roughly the same. The meaning is that there may well be more than three absorbers spread over the vertical branch of the curves in Fig. 12. The three ionization parameters considered here may represent some volume averaged properties of the entire cloud ensemble and the associated column densities are some total column densities of a large number of such clouds. Moreover, the largest U_{OX} component may provide the confining medium for the two other ionization components. Needless to say, real confined outflowing clouds are characterised by a more complicated density and pressure structure than with the simplified, constant density clouds considered here (see Chelouche & Netzer 2001).

The idea of pressure equilibrium of all absorbers can provide additional constraints

on the gas density and location in NGC 3783. Given the earlier limits on the density and location of the gas and assuming that all components are in pressure equilibrium in the same general location, we require that the distance of this region is at least 3.2 pc (the minimum distance of the lowest ionization component). However, this zone cannot be much further away because of total size and volume considerations. Under the assumed conditions, the highest ionization parameter component is the one with the lowest density and hence the largest dimension. However, its radial extent cannot exceed about 500 pc (the approximate radius of the narrow-line region) and thus its mean density cannot fall below about 10 cm^{-3}. Pressure equilibrium then dictates the density of the lowest ionization component and a maximum distance of about 25 pc. This limitation is only imposed on discrete clouds i.e. on the mean location dependent properties of the gas. Real absorbers may not be "clouds". They can cover a large range of distances and can have location dependent properties. The detailed investigation of such models is beyond the scope of the present paper.

4.4. The emission lines

There is no indication for flux variation in any of the observed emission lines. Here the uncertainty is rather large since the strongest lines are observed at the long wavelength poorer S/N range. We obtain satisfactory fits for most lines by assuming that the emission line gas has the same column density and ionization parameter as the absorbing gas. The required emission covering factors are 0.1–0.2 for the $\log(U_{OX}) = -2.4$ component , 0.07–0.15 for the $\log(U_{OX}) = -1.2$ component and ~ 0.1 for the $\log(U_{OX}) = -0.6$ component. The large range is due to the uncertainties in the continuum placement and in estimating the fraction of the O VII and O VIII emission lines that are being absorbed (the model shown in Figs. 7 and 8 assumes that *all* the emitted photons are seen through the absorbers).

A clear shortcoming of the model is the fitting of the intercombination O VII line whose calculated intensity is too small by a large factor (2-4). A big part of the discrepancy is due to the O VI λ21.87 Å absorption line situated close to this emission (Fig. 7). This may be related to the O VI problem discussed earlier or, perhas, to the assumption that all emission line photons are seen through the absorbers. We also note the difference between the absorption covering factor (0.8–1.0) and the emission covering factor (0.1–0.2). This may be related to a special geometry, e.g. a biconical flow or a torus geometry (e.g. Krolik & Kriss 2001). We did not investigate this possibility any further.

4.5. UV absorbers in NGC 3783

NGC 3783 contains a time variable UV absorber that has been described in various earlier publications (Gabel et al. 2003a and references therein). Our analysis clearly indicates that at least one X-ray component contains gas which is of low enough ionization to produce strong UV absorption lines of C IV, N V and O VI.

The predicted EWs of the UV lines depend on two factors that were given little attention in this work. The first is the exact shape of the UV continuum and the second the UV absorption covering fraction which can be different from the X-ray absorption covering factor. A UV continuum which is softer than the one assumed here can result in higher ionization of carbon, nitrogen and oxygen with little effect on most X-ray lines. This is very important for the C IVλ1549 Å and N Vλ1240 Å lines but less so for the UV lines of O VI that are directly linked to the O VI column density discussed here.

As for the UV covering factor, the size of the UV continuum source can be much larger than the size of the central X-ray source. This will result in saturated UV absorption lines whose EWs are smaller than the ones indicated by the column densities derived here, However, our upper limit on the density of the low ionization component, combined with its column density, suggest a very large line-of-sight dimension ($> 10^{17}$ cm). Assuming lateral dimension of the same size or large, we reach the conclusion that the physical dimension of this component is much larger than the expected dimension of any likely UV source (e.g. the surface of a thin accretion disk). A combined UV X-ray work, taking all those points into consideration, is in progress.

UV absorbers are also UV emitters and the low ionization component can contribute also to the observed UV emission lines. Our photoionization calculations show that this contribution is very small. For example, an emission covering factor of 0.1, similar to the one deduced from the X-ray emission lines, will produce O VIλ1035 line with emission EW of about 1Å.

4.6. The long wavelength component

Perhaps the most interesting result of this study is the appearance and disappearance of the soft excess component. This broad-band continuum source was seen in two of the six observations, that are, on average, the highest luminosity observations. While the increase in softness ratio with the source luminosity is well known and well documented in a number of AGN (e.g. Magdziarz et al., 1998; Chiang et al., 2000; Markowitz & Edelson 2001) we are not aware of a softness ratio increase that is *not associated* with an overall brightening of the

source. NGC 3783 seems to be the first AGN to show this phenomenon and we suspect that careful spectroscopic monitoring will reveal the same or a similar behavior in other sources. This has important consequences to the continuum production mechanism, as well as for the modeling of the warm X-ray gas around the center.

We do not know the origin of the soft continuum source. In particular, we do not have information on its $\lambda > 30$Å flux (the source was not in a high-state in any of the published *XMM-Newton* observations). It may be related to a broad band phenomenon, e.g. due a flaring accretion disk, or else a narrower band emission like a single temperature black body. Simple global energy consideration show that this phenomemnon is unrelated to the appearance of broad emission features like those claimed to be seen in at least two sources (Branduardi et al 2001; Mason et al. 2002) and interpreted as due to relativistic disk lines (see also Lee et al. 2002).

Finally, we must comment on the possibility of a more complicated behavior. Our analysis is based on the fitting of a single powerlaw continuum at low-state and the addition of a soft X-ray source during high state. However, an equivalent analysis could be carried out in a reversed order, i.e. starting from a pure powerlaw at high-state and *subtracting* a continuum component to explain the low-state spectrum. As argued earlier, the observed spectral changes at long wavelengths are too large to be explained by pure opacity variations and it is not at all clear what other mechanism could explain an AGN continuum with flux deficit at long wavelengths.

5. Conclusions

Our detailed measurements and analysis of the 900 ks data set of NGC 3783 lead to the following results:

1. The source fluctuates in luminosity, by a factor ~ 1.5, during individual 170 ks observations. The fluctuations are not associated with significant spectral variations.

2. On time scales of 20–120 days, the source exhibits two very different spectral shapes denoted here as the high and the low state spectra. The two are associated with different softness ratios that seem unrelated to the total X-ray luminosity. The observed changes in the underlying continuum can be described as due to the appearance and disappearance of a soft excess component. The origin of this continuum source is not clear. To the best of our knowledge, NGC 3783 is the first AGN to show such a behavior.

3. The appearnce of the soft continuum component can explain all observed spectral variation within the measurement uncertainties. There is no need to invoke opacity changes between the low and the high phases. This conclusion depend mostly on the S/N in the high state spectrum.

4. A combination of three ionization components, each split into two kinematic components, explains very well the intensity of almost all observed absorption lines and the bound-free absorption. The components span a large range of ionization and a total column of about 4×10^{22} cm^{-2}. The only real discrepancy is between the observed and the calculated strength of the iron M-shell UTA feature at 16–16.5Å. This is most likely due to inadequate dielectronic recombination rates used in the calculations. The largest other uncertainty is in the column density of O VI.

5. The three generic absorbers discussed in this work seem to have the same $n_e \times T$ and we speculate that they may be in pressure equilibrium with each other, occupying the same volume in the nucleus. This is the first confirmation of the location of several X-ray absorbers on the vertical part of the $\log(T)$ vs. $\log(U_{OX}/T)$ stability curve of AGN.

6. We have obtained thee lower limits on the gas distance from the center, corresponding to our three generic absorbers. The limits are 3.2 pc, 0.6 pc and about 0.2 for the low ionization, intermediate ionization and high ionization absorbers, respectively. The pressure equilibrium assumption indicates an upper limit to the distance of the low ionization absorber of about 25 pc.

This work is supported by the Israel Science Foundation grant 545/00, E.B. was supported by the Yigal-Alon Fellowship and by the GIF Foundation under grant #2028-1093.7/2001. We gratefully acknowledge the financial support of CXC grant GO1-2103 (S. K., W. N. B., I. M. G.), NASA LTSA grant NAG 5-13035 (S. K., W. N. B.) and the Alfred P. Sloan Foundation (W. N. B.),

REFERENCES

Arav, N., Becker, R. H., Laurent-Muehleisen, S. A., Gregg, M. D., White, R. L., Brotherton, M. S., & de Kool, M. 1999, ApJ, 524, 566

Arav, N., Korista, K. T., & de Kool, M. 2002, ApJ, 566, 699

Barlow, T. A. & Sargent, W. L. W. 1997, AJ, 113, 136

Barlow, T. A., Hamann, F., & Sargent, W. L. W. 1997, ASP Conf. Ser. 128: Mass Ejection from Active Galactic Nuclei, 13

Behar, E., & Netzer, H. 2002, ApJ, 570, 165

Behar, E., Sako, M., & Kahn, S. M. 2001, ApJ, 563, 497

Behar, E. & Kahn, S. M. 2002, NASA Laboratory Astrophysics Workshop, Ed. Farid Salama (astro-ph/0210280)

Behar et al., 2003 (submitted to ApJ)

Blustin, A. J., Branduardi-Raymont, G., Behar, E., Kaastra, J. S., Kahn, S. M., Page, M. J., Sako, M., & Steenbrugge, K. C. 2002, A&A, 392, 453

Branduardi-Raymont, G., Sako, M., Kahn, S. M., Brinkman, A. C., Kaastra, J. S., & Page, M. J. 2001, A&A, 365, L140

Chelouche, D. & Netzer, H. 2001, MNRAS, 326, 916

Chelouche, D. & Netzer, H. 2003, MNRAS, (in press)

Chiang, J., Reynolds, C. S., Blaes, O. M., Nowak, M. A., Murray, N., Madejski, G., Marshall, H. L., & Magdziarz, P. 2000, ApJ, 528, 292

Gabel, J. R. et al. 2003a, ApJ, 583, 178

Gabel, J. R. et al. 2003b, ApJ, (in press)

George, I. M., Turner, T. J., Mushotzky, R., Nandra, K., & Netzer, H. 1998, ApJ, 503, 174

Hess, C. J., Kahn, S. M., & Paerels, F. B. S. 1997, ApJ, 478, 94

Kaspi, S., Brandt, W. N., Netzer, H., Sambruna, R., Chartas, G., Garmire, G. P., & Nousek, J. A. 2000a, ApJ, 535, L17

Kaspi, S. et al. 2001, ApJ, 554, 216

Kaspi, S., et al. 2002, ApJ, 574, 643

Kinkhabwala, A. et al. 2002, ApJ, 575, 732

Komossa, S. & Fink, H. 1997, A&A, 322, 719

Komossa, S. & Meerschweinchen, J. 2000, A&A, 354, 411

Kraemer, S. B., Crenshaw, D. M., & Gabel, J. R. 2001, ApJ, 557, 30

Krolik, J. H., & Kriss, G. A. 2001, ApJ, 561, 684

Lee, J. C., Ogle, P. M., Canizares, C. R., Marshall, H. L., Schulz, N. S., Morales, R., Fabian, A. C., & Iwasawa, K. 2001, ApJ, 554, L13

Magdziarz, P., Blaes, O. M., Zdziarski, A. A., Johnson, W. N., & Smith, D. A. 1998, MNRAS, 301, 179

Markowitz, A. & Edelson, R. 2001, ApJ, 547, 684

Marshall, F. E. et al. 1993, ApJ, 405, 168

Mason, K. O. et al. 2003, ApJ, 582, 95

Mathur, S., Elvis, M., & Wilkes, B. 1995, ApJ, 452, 230

Netzer, H. 1996, ApJ, 473, 781

Netzer, H., Chelouche, D., George, I. M., Turner, T. J., Crenshaw, D. M., Kraemer, S. B., & Nandra, K. 2002, ApJ, 571, 256

Pradhan, A. K. 2000, ApJ, 545, L165

Reynolds, C. S. & Fabian, A. C. 1995, MNRAS, 273, 1167

Savin, D. W. et al. 2002, ApJ, 576, 1098

Steenbrugge, K.C. et al. 2003, A&A, 402, 477

Table 1. Equivalent Widths[a]

Ion & Line	low state	high state	Kaspi et al. (2002)
Si XIV λ6.182	20.4 ± 1.2	22.6 ± 1.7	20.5 ± 0.8
Si XIII λ6.648	16.0 ± 1.3	14.6 ± 1.3	14.9 ± 0.7
Si XII λ6.718[b]	2.9 ± 0.5	3.8 ± 0.7	3.0 ± 0.4
Si XI λ6.778	4.8 ± 0.8	5.9 ± 1.2	4.8 ± 0.6
Si X λ6.859	10.6 ± 1.1	9.4 ± 1.4	10.9 ± 0.8
Si IX λ6.931	7.2 ± 1.0	7.7 ± 1.6	7.1 ± 0.7
Si VIII λ6.999	4.3 ± 1.0	4.4 ± 1.4	4.3 ± 0.8
S XVI λ4.729	11.5 ± 1.6	11.6 ± 2.5	10.7 ± 1.2
S XV λ5.039	8.7 ± 1.7	9.1 ± 2.5	9.2 ± 1.2

[a]Equivalent widths were measured as described in Paper I and are given in mÅ.

[b]This line is blended with Mg XII λ6.738 with 1:1 ratio. Tabulated values are only for the Si XII λ6.718 line.

Table 2. Column Densities[a]

Ion & Line	measured[b]	model $\log(U_{ox})$ −2.4	−1.2	−0.6	total
Si XIV λ6.182	> 17.50[c]	···	···	···	···
Si XIV λ5.217	17.94 ± 0.10	···	···	···	···
Si XIV λ4.947	17.83 ± 0.20	···	···	···	···
Si XIV adopted value	17.90 ± 0.20	12.50	17.00	17.48	17.60
Si XIII λ6.648	> 16.87[c]	···	···	···	···
Si XIII λ5.681	> 17.23[c]	···	···	···	···
Si XIII λ5.405	17.57 ± 0.20	···	···	···	···
Si XIII λ5.286	17.71 ± 0.25	···	···	···	···
Si XIII adopted value	17.65 ± 0.20	14.68	17.31	16.94	17.46
Si XII λ6.718	16.10 ± 0.06	15.57	16.55	15.41	16.62
Si XI λ6.778	16.29 ± 0.06	16.43	16.15	14.11	16.61
Si X λ6.859	16.83 ± 0.05	16.90	15.88	13.10	16.94
Si IX λ6.931	16.66 ± 0.06	17.04	15.27	11.68	17.05
Si VIII λ6.999	16.66 ± 0.08	16.81	14.26	9.93	16.81
Si VII λ7.063	16.26 ± 0.20	16.13	12.71	7.80	16.13
S XVI λ4.729	> 17.29[c]	···	···	···	···
S XVI λ3.991	17.58 ± 0.13	···	···	···	···
S XVI adopted value	17.58 ± 0.13	10.13	16.23	17.16	17.21
S XV λ5.039	16.87 ± 0.09	···	···	···	···
S XV λ4.299	17.08 ± 0.25	···	···	···	···
S XV adopted value	17.00 ± 0.20	12.70	16.90	17.00	17.25
Mg VIII λ9.506	16.58 ± 0.05	16.77	14.46	11.13	16.77
Mg IX λ9.378	16.39 ± 0.06	17.06	15.13	12.61	17.07
O VIII λ14.821	18.67 ± 0.25	···	···	···	···
O VIII λ14.634	18.59 ± 0.14	···	···	···	···
O VIII adopted value	18.63 ± 0.25	17.65	18.05	17.55	18.28
O VII λ17.396	18.03 ± 0.20	···	···	···	···
O VII λ17.200	18.04 ± 0.20	···	···	···	···
O VII adopted value	18.04 ± 0.20	18.39	16.84	15.49	18.40
O VI λ21.01	> 16.42[c]	···	···	···	···
O VI λ19.341	> 17.00[c]	···	···	···	···
O VI adopted value	> 17.00	17.96	14.34	12.23	17.96
O V λ22.334	> 16.34[c]	···	···	···	···
O V λ19.924	17.07 ± 0.40	···	···	···	···
O V adopted value	17.07 ± 0.40	17.54	12.59	9.3	17.54

[a]Log of column density in units of cm^{-2}.

[b]Column densities and uncertainties derived from the EWs in Paper I. The EW was divided in the ratio 1:0.7, then the column density corresponding to the 1/1.7 part was computed assuming a Doppler width of 250 km s^{-1}. The derived column density was multiplied by 1.7 to result with the total column density listed here. Uncertainties were calculated from the EWs uncertanties. See text for details.

[c]Saturated line, lower limit only.

Table 3. Parameters of Generic Models

Model	$\log(U_{OX})$	$\log(N)$
Low ionization	-2.4	21.9
Intermidiate ionization	-1.2	22.0
High ionization	-0.6	22.3

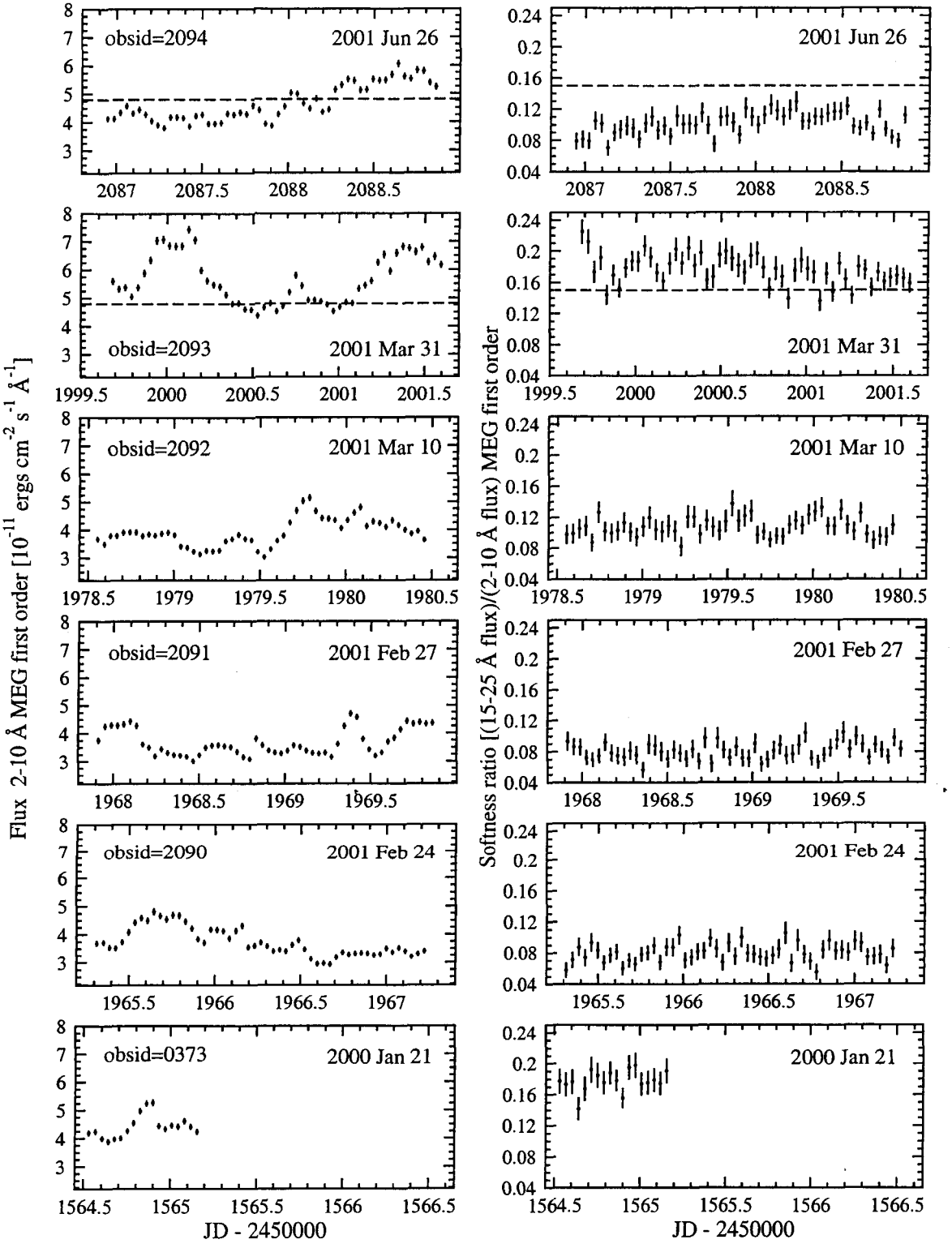

Fig. 1.— MEG 2–10 Å flux light curves (left) and softness ratios (ratio of the 2–10 and the 15–25 Å count rates, right) for all *Chandra* observations of NGC 3783. The dashed lines across observations no. 2093 and 2094 represent constant flux (4.8) and softness ratio (0.15). They illustrate the fact that similar 2–10 Å fluxes (middle part of obs. 2093 and last part of obs. 2094) can be associated with very different softness ratios.

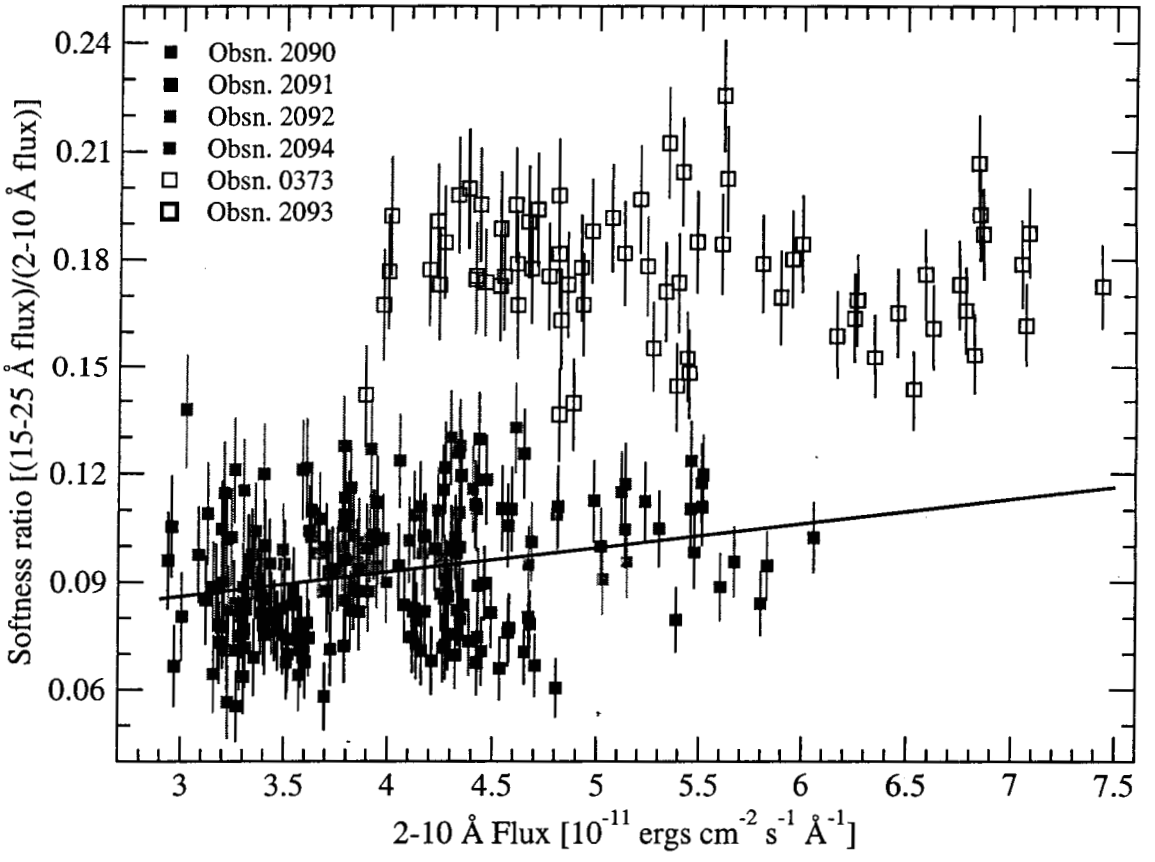

Fig. 2.— Softness ratio vs. 2–10 Å flux for the data in Fig. 1. The low and high-state observations are shown as filled and open symbols, respectively, and the various observations are denoted with different colors. The solid straight line is the linear regression fit to the low-state observations. No significant correlation of softness ratio vs. flux was found for the high state observations.

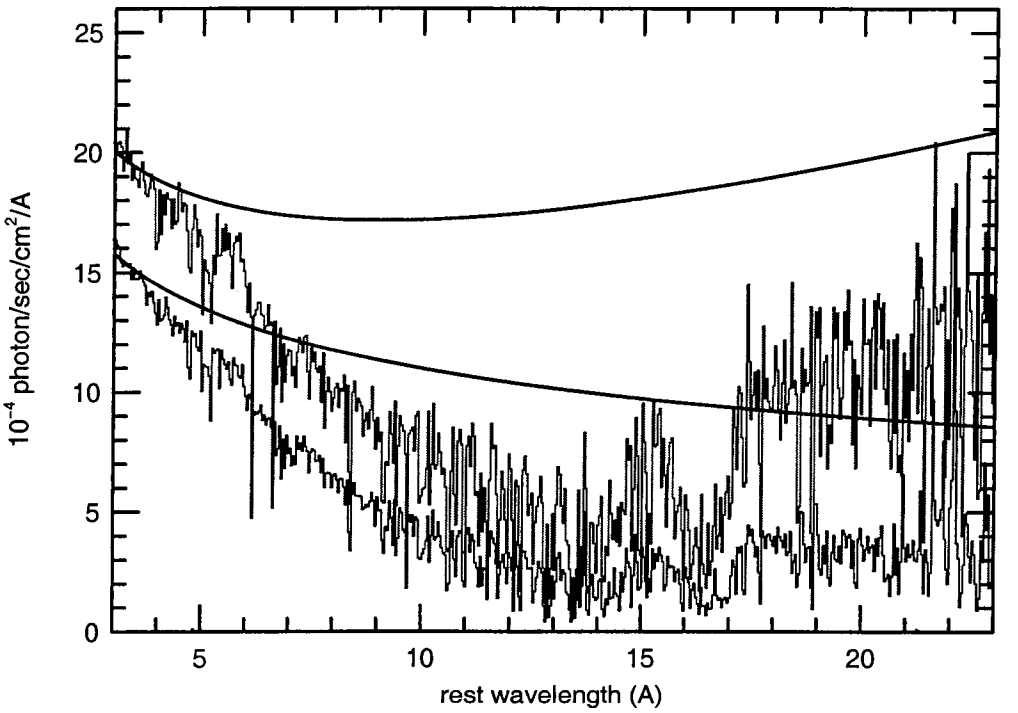

Fig. 3.— High-state (red, observations 0373 and 2093 combined) and low-state (blue, all other observations combined) spectra of NGC 3783 binned to 0.04 Å. The solid lines are the two chosen intrinsic continua (see text). The lower continuum is a single power-law with $\Gamma = 1.6$. The high continuum is made out of two power-laws with slopes $\Gamma = 1.6$ and $\Gamma = 3.2$ and relative normalization of 1:0.4 at 1 keV.

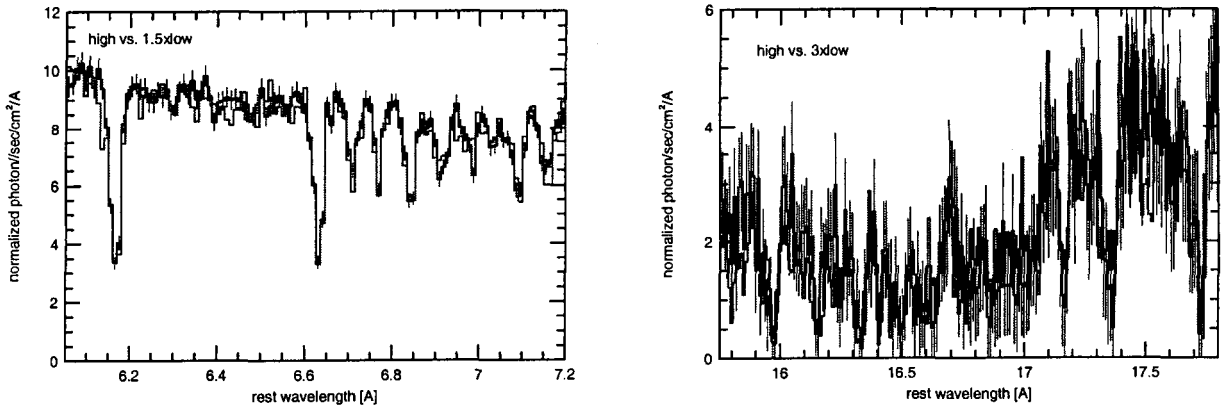

Fig. 4.— Left: High-state (red) vs. low-state (blue) 6–7 Å spectra of NGC 3783 showing the great similarity in absorption line EWs (cf. table 1). The low-state spectrum was multiplied by 1.5 to match the flux of the high-state continuum. For clarity, error bars are only plotted for the low state spectrum. Right: Same for the 15.6–18 Å range except for the different scaling of the low-state continuum.

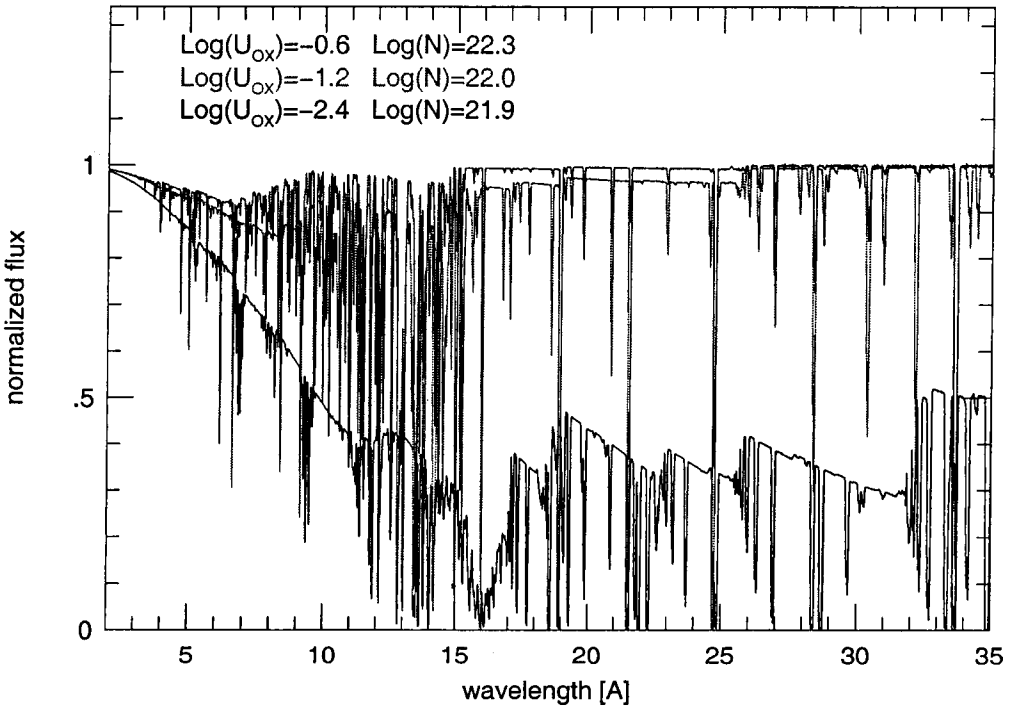

Fig. 5.— The three generic components that were used to model the low-state spectrum of NGC 3783. All components are shown on the same normalized scale where 1 is the incident continuum level.

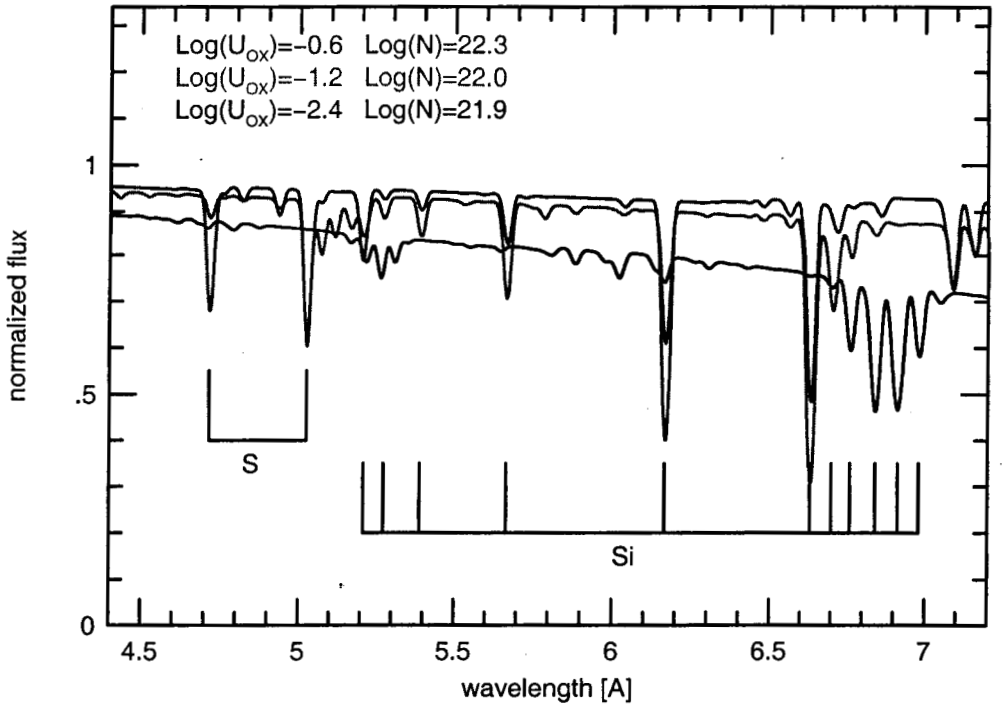

Fig. 6.— A blown up version of Fig. 5 showing the 4.5–7 Å region used to constrain the model parameters (see text). Note that all three models are required to explain the large range of ionization (from Si VII to S XVI.)

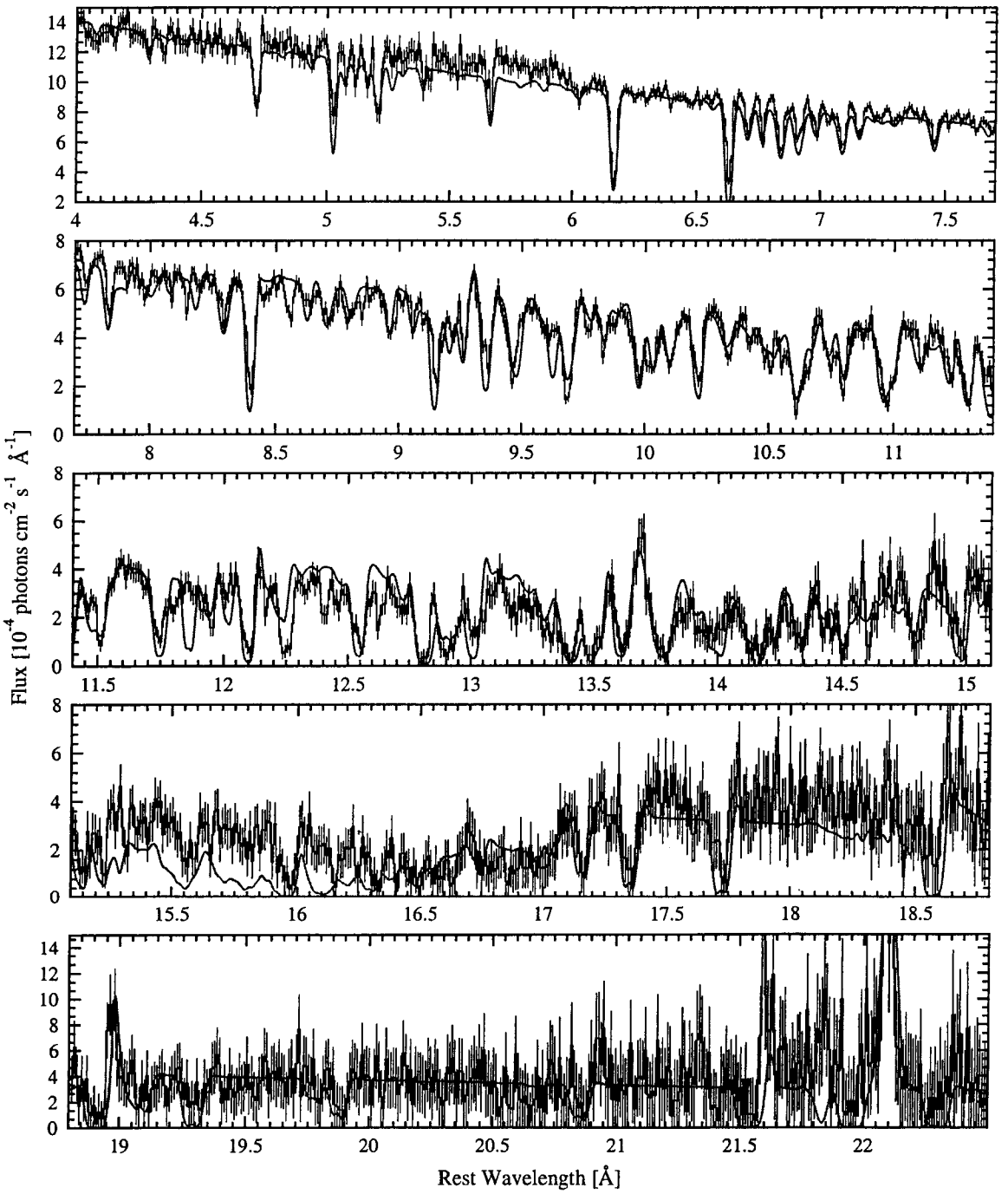

Fig. 7.— A comparison of the low state spectrum with the six component model (three ionization components each split into two kinematic components). Note that most of the apparent discrepancy at around 5–6 Å is due to a known calibration problem (H. Marshall, private communication).

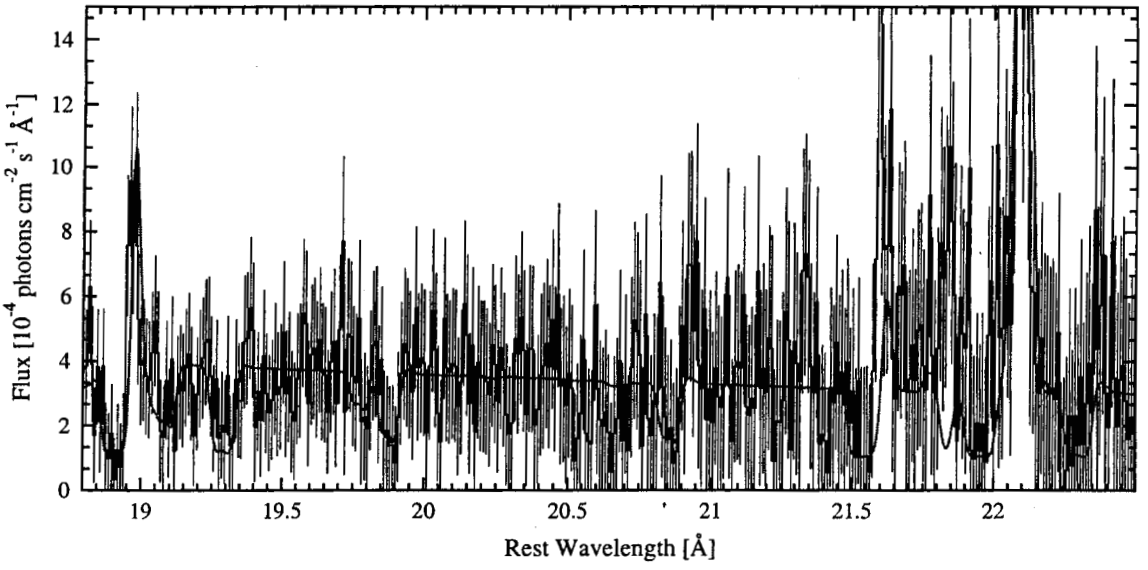

Fig. 8.— Model vs. observation for the long wavelength spectrum assuming $\Gamma = 1.5$ and a line-of-sight covering factor of 0.85 for all absorbers.

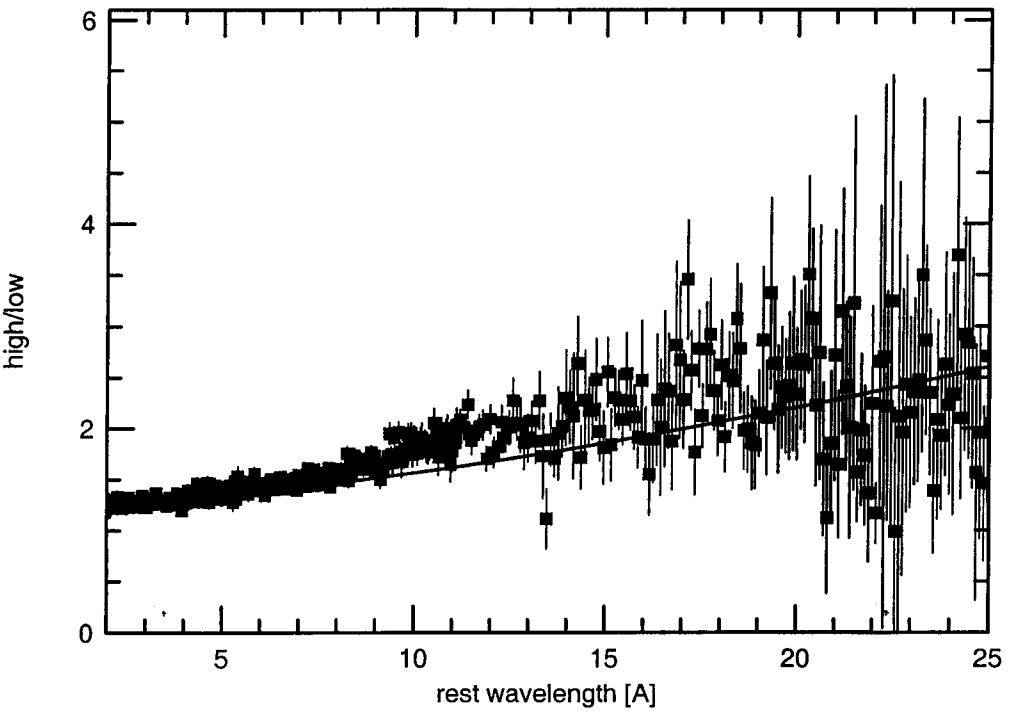

Fig. 9.— A ratio spectrum of NGC 3783: Points with error bars are the result of dividing the high-state spectrum by the low-state spectrum. The binning is 0.04Å for $\lambda < 11$Å and 0.1Å at longer wavelengths. The smooth line is the same division applied to the two continua shown in Fig. 3.

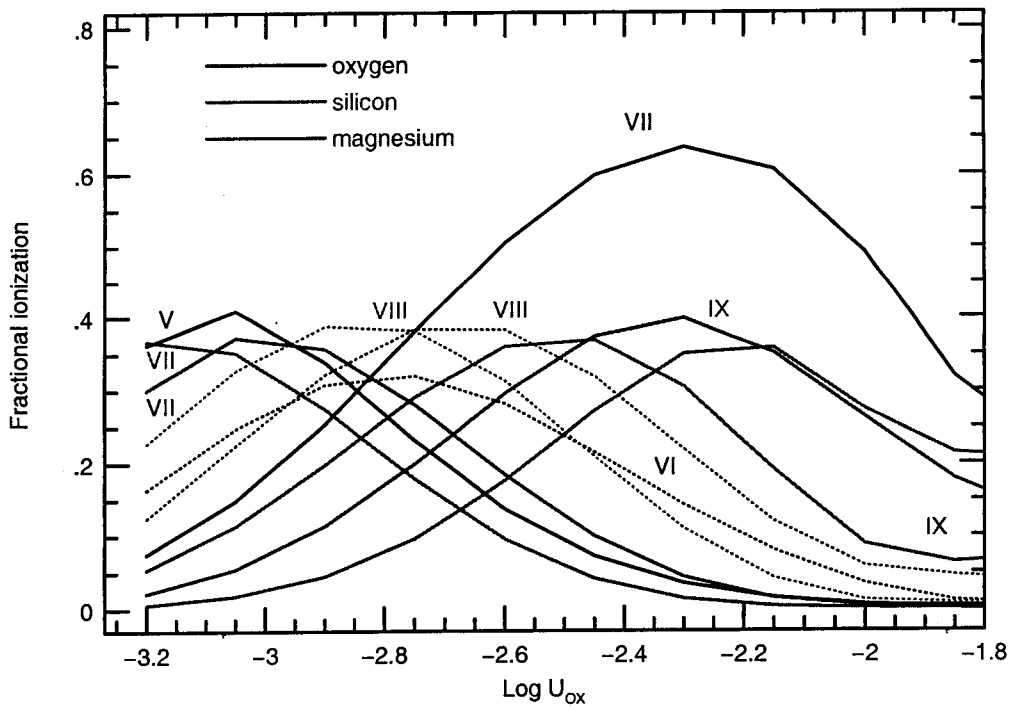

Fig. 10.— The fractional ionization of oxygen, magnesium and silicon ions in a low density gas of our chosen composition exposed to the NGC 3783 low-state continuum. The curves show the mean ionization of various ions averaged over a column density of $10^{21.5}$ cm^{-2}. Note the great similarity in the ionization of O VI, Mg VIII and Si VIII (all plotted with dotted lines).

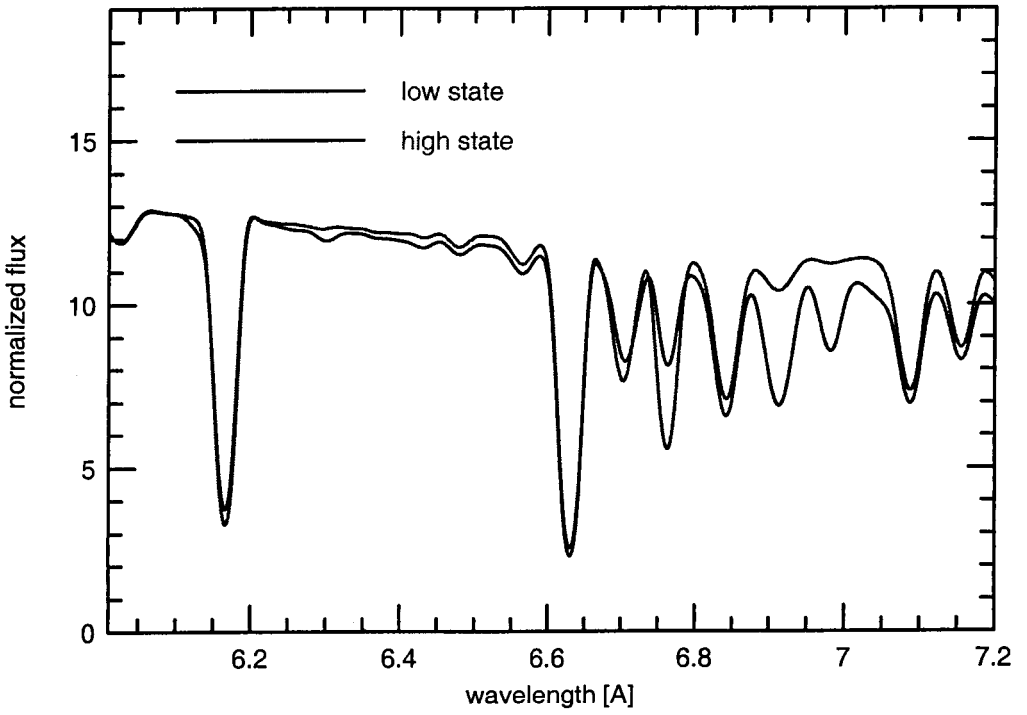

Fig. 11.— Low state and high state theoretical spectra assuming the observed variable NGC 3783 continuum and line of sight gas that responds instantly to continuum variations. The low state model (in blue) is the one described earlier and shown in Fig. 7. The high state spectrum (in red) assumed the high state SED discussed in the text. Such a continuum results in much weaker Si VIII and Si IX lines.

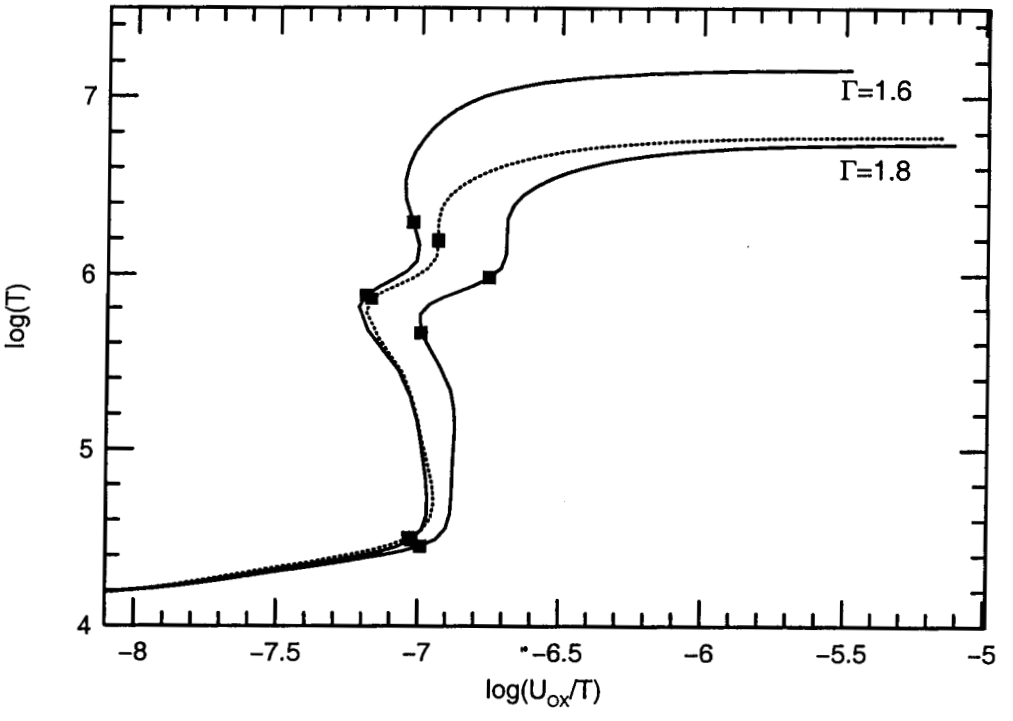

Fig. 12.— Thermal stability curves for a low density gas exposed to the low-state continuum of NGC 3783. The two curves marked by Γ are for a bare continuum with a 0.1–50 keV slope as marked. The dotted line is the stability curve for a gas exposed to the $\Gamma = 1.8$ continuum seen through the $\log U_{OX} = -2.4$ absorber. Points represent the location of the three absorbers considered in this work. All ionization components considered in this work are situated on the thermally stable part and they all have roughly the same gas pressure.